

Topology-Preserving Segmentation Network

Han Zhang, Lok Ming Lui

Abstract—Medical image segmentation aims to extract anatomical or pathological structures in the human body. Most structures of interest are of similar patterns. For example, the relative location and size of the lung and kidney differ little among subjects. Incorporating these morphology rules as prior knowledge into the segmentation model is believed to be an effective way to enhance the accuracy of the segmentation. Motivated by this, we propose the Topology-Preserving Segmentation Network(TPSN), which can predict segmentation masks with the same topology prescribed for specific tasks. TPSN is a deformation-based model that yields a deformation map through an encoder-decoder architecture to warp the template masks to enclose the region of interest. In our framework, we propose the ReLU Jacobian regularization to enforce the bijectivity of the deformation. As such, the predicted mask by TPSN has the same topology as the template mask. To further enhance the accuracy, we propose the multi-level TPSN(mlTPSN) that produces masks using a coarse-to-fine strategy. In addition, our proposed model is incorporated with a loss based on the Chan-Vese model for unsupervised segmentation. Our TPSN is capable of segmenting objects with different topologies. In the experiments, we evaluated the performance of our model on KiTS21 dataset for simply-connected kidney segmentation and the ACDC dataset for the doubly-connected left ventricle wall segmentation. For multiple objects segmentation, we test the proposed method on BTCV dataset. Experimental results illustrate that our methods can achieve significantly better than other state-of-the-art pixel-wise and deformation-based segmentation models.

Index Terms—Topology-Preserving , Prior Knowledge , Deformable Model , Medical Image Segmentation, Unsupervised Segmentation

I. INTRODUCTION

The segmentation of anatomical structures is an essential procedure for many clinical applications, such as diagnosing diseases and monitoring disease progression. Image segmentation has been widely studied and many segmentation models have been developed. Recent years have also witnessed the tremendous success of learning-based frameworks for image segmentation [1], [2]. In the case of medical images, most anatomical structures are commonly located at nearby positions of the human body and are usually geometrically similar. For instance, anatomical structures like the kidney or liver are known to be simply-connected while the vessel walls are known to be circular shaped. Nevertheless, conventional segmentation methods usually do not incorporate geometric information, and thus these priori geometric constraints cannot be satisfied. For instance, most deep learning segmentation models based on pixel-wise classification may easily give inaccurate segmentation results with topological errors, e.g., isolated segmented regions in the stomach and holes in the

vessel wall. Such inaccuracies could be clinically problematic and impractical[3]. To alleviate this issue, prior knowledge about the morphological rules that organs should obey can be taken into consideration for better segmentation quality. For this purpose, some recent works incorporate prior shape information into the regularization term [4]. These models can improve the segmentation results, although there is no guarantee on topological correctness. On the other hand, deformation-based segmentation models, which warp a template image to a target domain that encloses the region of interest, are suitable for enforcing topological and geometric constraints. For instance, quasiconformal segmentation models have been recently proposed, which deform a template shape by a quasiconformal mapping to segment the image [5], [6]. Topological and convexity constraints can be enforced by controlling the properties of the quasiconformal mapping. To integrate data information and enhance efficiency, learning-based imaging models have attracted much attention in recent years. Using U-Net[7], the dense spatial transformation can be generated by deep neural network models[8]. This paves the way to develop learning-based segmentation based on deformable models. The challenge is how the geometric constraints on the deformation map can be enforced within the deep neural network. Recent works explore different regularizations to be imposed on the output of a spatial transformer network or its sub-layers. However, these works are usually either over-constrained, causing sub-optimal results [3] or lacking mathematical justifications to guarantee a solution satisfying the prescribed geometric constraints[9].

In this paper, we propose a learning-based topology-preserving segmentation framework, which learns to segment an input image by deforming the template masks to enclose the region of interest. We propose a novel ReLU Jacobian regularizer, which plays an important role in enforcing the topological constraint. The ReLU Jacobian is simply the negative of the Jacobian determinant activated by the ReLU function. Minimizing this loss can prevent the change of orientation under the deformation map in the segmentation model. The topology of the output mask is therefore guaranteed to be the same as that of the input prior mask.

Our proposed framework has been evaluated by extensive experiments. The proposed model is firstly applied for supervised segmentation, in which the segmentation network is trained using a collection of images with labeled masks. The loss function, in this case, comprises the proposed ReLU Jacobian regularization and the pixel-wise segmentation loss, such as the Dice score. As expected, our proposed network can output segmentation results with the prescribed topological guarantee. In this paper, the simply-connected and doubly connected object segmentation models are evaluated on the KiTS21[10] and ACDC[11] dataset, respectively. Besides, to

H. Zhang is with the City University of Hong Kong, Hong Kong (e-mail:h Zhang863-c@my.cityu.edu.hk).

L.M. Lui is with the Chinese University of Hong Kong, Hong Kong (e-mail: lmlui@math.cuhk.edu.hk). Corresponding author.

extend the model to segment more general multiply-connected objects, the Fill First, Dig Second (FFDS) strategy is designed. To further improve the segmentation accuracy, we propose a multi-level TPSN architecture that predicts the segmentation mask from a coarse-to-fine fashion. In addition, our proposed model is applied for unsupervised segmentation. The Dice score is replaced by the segmentation term adopted from the Chan-Vese segmentation model [12] in the loss function. Our experiments show encouraging results using the proposed unsupervised segmentation network. Last but not least, our proposed framework is also tested on BTCV [13] dataset from MICCAI 2015 challenge for the segmentation of multiple objects. Experimental results are also promising. To the best of our knowledge, this is the first deformation-based segmentation network to segment multi-objects simultaneously.

II. RELATED WORK

A. Image Segmentation

Image segmentation has been studied extensively and various segmentation models have been developed in recent years. The active contour model [14] is perhaps the earliest segmentation model, which evolves a parameterized curve iteratively to the object boundary. Later, Chan *et al.* [12] proposed the active contour model without edge, based on the Mumford-Shah functional and level sets, to segment an image by curve evolution. The model has an advantage of allowing topology change. Another earlier work performed segmentation by the technique of k -mean clustering that sorts pixels to k different clusters [15]. With the popularity of deep learning in recent years, a lot of segmentation models using deep architectures have been invented. Ronneberger *et al.* [7] proposed the learning-based segmentation model using the U-Net structure and achieved impressive results. The extension of U-Net for 3D volumetric images was later developed in [16], [17]. To improve the framework, Zhou *et al.* [18] re-designed the skip connection to reduce the semantic gap between the feature maps of the encoders and decoders. As learning-based segmentation models require data, multiple works have been devoted to generating meaningful training data. A series of dataset [19], [11], [10], [13] are organized and open to the public for research purposes. Some works design learning-based segmentation models by manipulating data. For instance, a segmentation framework, called nnUNet, was proposed in [20], which uses only a standard U-Net architecture with a series of practical pre- and post- processing strategies on the images. This framework achieved outstanding results on multiple segmentation datasets. More learning-based models have been invented recently by adjusting the network architectures. Jha *et al.* [1] proposed to use one UNet to predict an initial mask and apply an additional one to refine the segmentation result. Farshad *et al.* proposed the Y-net, which contains two encoders in the architecture for image segmentation. Hatamizadeh *et al.* [21] build up a U-shaped segmentation transformer based on vision transformer [22].

Besides, unsupervised learning-based segmentation models have also been considered, which train the model by images without labeled masks as the ground truth. Ouali *et al.* [23] proposed the autoregressive unsupervised image segmentation

model by maximizing the mutual information between different constructed views. Kim *et al.* [24] proposed an unsupervised learning framework for image segmentation, using the intensity similarity loss and spatial continuity loss.

B. Deformable Model

Deformable models for image segmentation have also been explored by different research groups. The main idea of deformable segmentation models is to obtain the result by searching for a suitable deformation. The active contour model [14] can be considered as a deformable model, which deforms a collection of points discretizing a curve to enclose the boundary of the object. Cootes *et al.* [25] extended the active contour model to a learnable model by extracting the main pattern of variations using principle component analysis (PCA). More recent deformable image segmentation models consider a dense spatial deformation map between the template image and the target image. The template mask is then deformed to the shape of the object in the image. For instance, Chan *et al.* [5] proposed a deformation-based segmentation model using quasiconformal maps and the segmentation results are guaranteed to be topology-preserving. Siu *et al.* [6] applied the dihedral angle in the deformable model for image segmentation to incorporate the partial convexity and topology constraints. Zhang *et al.* [26] proposed a deformable model using the hyperelastic regularization, which gives rise to a topology-preserving segmentation model and can be applied to 3D volumetric images. Convexity prior is further integrated into the model in [27]. Learning models based on the idea of deformable models have attracted more attention [28], [29] since the spatial transformer network are proposed [8]. Lee *et al.* [9] applied the laplacian regularization to regularize the final output, which can better preserve the topology of the template. Wyburd *et al.* [3] proposed a topology-preserving deep segmentation network by compositing a series of bijection deformations. Nevertheless, these methods generally may either fail to have a mathematical guarantee of topological preservation or yield sub-optimal results due to the over-constrained problem, especially for the segmentation of structures with complex geometry.

C. Prior Information In Neural Network

The incorporation of prior information into the deep neural network has been considered recently. The main strategy is to design a suitable loss function that integrates the prior knowledge to regularize the predicted mask. Mosinska *et al.* [30] define a topological loss that is aware of the higher-order topological features of linear structures. Zhou *et al.* [31] proposed a segmentation model, which took into consideration of the relative location and size statistically. The proposed model performed well in multi-organ segmentation. Hu *et al.* [32] designed a continuous-valued loss function to enforce the topological correctness via computational topology theories. Shit *et al.* [33] introduced cIDice to measure the Dice of the skeletons between the prediction and the ground truth for tubular structures. Clough *et al.* [34] proposed to use the differentiable persistent homology to drive the segmentations process to give an output with a prescribed Betti number.

III. METHOD

In this section, we describe our proposed segmentation framework in detail. Conventional learning-based segmentation approaches are commonly formulated as a pixel-wise classification problem, with which the topological constraint is hard to be integrated. In this work, we train a network that can produce a diffeomorphism to segment the input image by warping the template mask.

A. Grid Parameterization and Spatial Transformation

To make it convenient for spatial transformation, the image domain is first parameterized to a standard grid. Consider an image of size $H \times W \times D$, we parameterize it into a standard domain $[-1, 1] \times [-1, 1] \times [-1, 1]$. The standard domain is discretized by a regular grid by $G = \{(x_i, y_j, z_k)\} = \{(ih_x - 1, jh_y - 1, kh_z - 1) : i = 0, 1, \dots, H - 1; j = 0, 1, \dots, W - 1; k = 0, 1, \dots, D - 1\}$, where $h_x = \frac{2}{H-1}$, $h_y = \frac{2}{W-1}$ and $h_z = \frac{2}{D-1}$.

A dense spatial transformation transforms a source image grid into a target image grid. In this paper, the source image grid is denoted by $G_s = \{(x_i^s, y_j^s, z_k^s)\} = G$. Denote the displacement vector field of the transformation by $V = \{(vx_i, vy_j, vz_k)\}$. The source image grid is then transformed to a target grid, which is denoted by $G_t = \{(x_i^t, y_j^t, z_k^t)\}$. More specifically, the coordinates of the target grid are given by the following formula:

$$\begin{aligned} x_i^t &= x_i^s + vx_i \\ y_j^t &= y_j^s + vy_j \\ z_k^t &= z_k^s + vz_k \end{aligned} \quad (1)$$

Denote the mapping from the source grid G_s to the target G_t by $f : (x_i^s, y_j^s, z_k^s) \mapsto (x_i^t, y_j^t, z_k^t)$, we can write the spatially transformed image grid as $J = I \circ f$

It is evident that the coordinates of the target grid G_t cannot match the standard grid of the regular image grid. A resampling method is then used to interpolate the intensity value to obtain a transformed image defined on the standard grid, which can be done as follows.

$$\begin{aligned} J(x_i, y_j, z_k) &= \sum_{n=0}^{H-1} \sum_{m=0}^{W-1} \sum_{p=0}^{D-1} I(x_n, y_m, z_p) \times k(x_i^t - x_n; \Phi_x) \\ &\quad \times k(y_j^t - y_m; \Phi_y) \times k(z_k^t - z_p; \Phi_z) \end{aligned} \quad (2)$$

where $(x_i, y_j, z_k) \in G$, Φ_x and Φ_y are the parameters of a generic sampling kernel $k(\cdot)$, $G_0 = \{(x_n, y_m, z_p)\} = G$ is a regular and normalized grid that discretizes the image domain of I . In this work, trilinear interpolation is used for 3D images,

while bilinear interpolation is used for 2D images. For 3D images, trilinear interpolation can be written as:

$$\begin{aligned} J(x_i, y_j, z_k) &= \sum_{n=0}^{H-1} \sum_{m=0}^{W-1} \sum_{p=0}^{D-1} I(x_n, y_m, z_p) \\ &\quad \times \max(0, 1 - \frac{|x_i^t - x_n|}{h_x}) \\ &\quad \times \max(0, 1 - \frac{|y_j^t - y_m|}{h_y}) \\ &\quad \times \max(0, 1 - \frac{|z_k^t - z_p|}{h_z}) \end{aligned} \quad (3)$$

where $(x_i, y_j, z_k) \in G$. The derivatives of transformed image J under the trilinear interpolation can be calculated by:

$$\begin{aligned} \frac{\partial J}{\partial I(x_n, y_m, z_p)}(x_i, y_j, z_k) &= \max(0, 1 - \frac{|x_i^t - x_n|}{h_x}) \\ &\quad \times \max(0, 1 - \frac{|y_j^t - y_m|}{h_y}) \\ &\quad \times \max(0, 1 - \frac{|z_k^t - z_p|}{h_z}) \end{aligned} \quad (4)$$

and

$$\begin{aligned} \frac{\partial J}{\partial x_i}(x_i, y_j, z_k) &= \sum_{n=0}^{H-1} \sum_{m=0}^{W-1} \sum_{p=0}^{D-1} I(x_n, y_m, z_p) \\ &\quad \times h(x_i^t) \times \max(0, 1 - \frac{|y_j^t - y_m|}{h_y}) \\ &\quad \times \max(0, 1 - \frac{|z_k^t - z_p|}{h_z}) \end{aligned} \quad (5)$$

where

$$h(x_i^s) = \begin{cases} 0 & \text{if } |x_p - x_i^s| \geq h_x \\ \frac{1}{h_x} & \text{if } x_p \geq x_i^s > x_p - h_x \\ -\frac{1}{h_x} & \text{if } x_p < x_i^s < x_p + h_x \end{cases} \quad (6)$$

The derivatives $\frac{\partial J}{\partial y_j^s}$ and $\frac{\partial J}{\partial z_k^s}$ can be computed similarly using Equation (5) and Equation (6).

B. Building Block

Network Architecture The architecture of our proposed Topology Preserving Segmentation Network (TPSN) is depicted in Fig. 1. The TPSN concatenates the image I to be segmented with the template mask M_{temp} and takes it as the input. The template mask is pre-defined according to the topological prior (e.g. a disk for the simply-connected prior, a circular annulus for the doubly-connected prior). Using an encoder-decoder network, a mapping $f = \mathcal{N}(I, M_{temp})$ is generated to warp the template mask into the final predicted mask $M_{pred} = M_{temp} \circ f$. During the training process, the proposed ReLU Jacobian regularization is used, which aims to preserve the orientation of the mapping. As a result, the transformed mask shares the same topology with the template mask.

Jacobian and Laplacian Regularization A key feature of our proposed framework is its ability to enforce the topological prior. Our strategy to preserve the topology is to learn a suitable bijective deformation map to transform a template mask

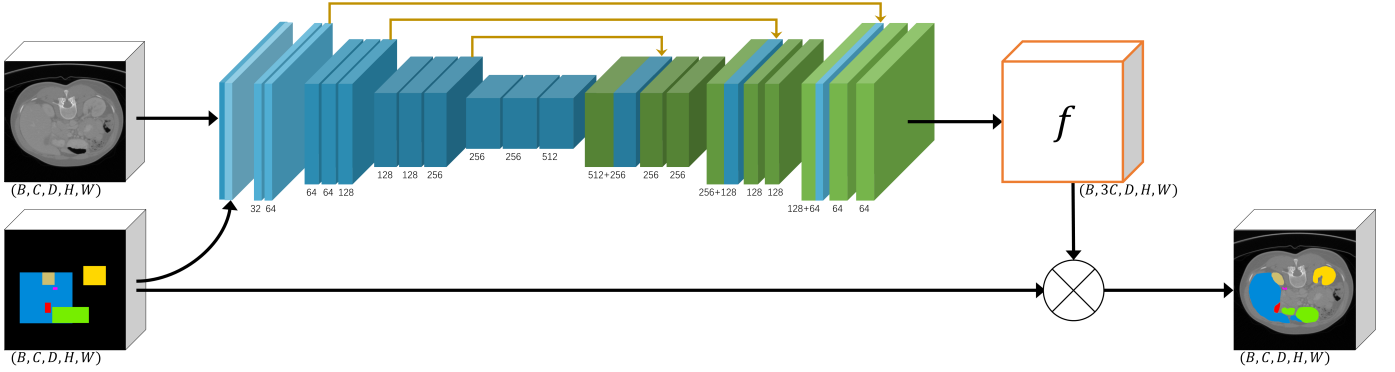


Fig. 1: The network architecture for TPSN. The prior and images are firstly concatenated and input to an encoder-decoder to produce a mapping. The mapping is then applied to deform the prior masks to enclose the regions of interest.

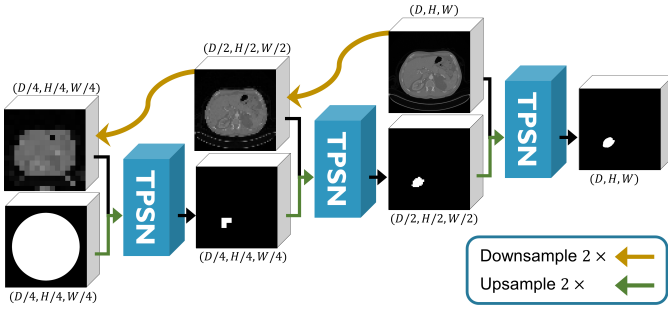


Fig. 2: Illustration for multi-level TPSN. The original images are downsampled into low-resolution and input into a TPSN with the prior in the same size. The predicted masks will be upsampled and used as the prior masks in the next layer.

into a deformed mask that segments the object in the image. The bijectivity of the deformation map ensures topological preservation. To achieve this goal, a suitable loss function is necessary. More specifically, the loss function \mathcal{L} should be capable of enforcing the diffeomorphic property of the output deformation map, while ensuring that M_{pred} is close to the ground truth segmentation result from the training data. In this paper, we propose the following loss function \mathcal{L} , which comprises a fidelity term and a regularization term. The fidelity term is chosen as the Dice loss for supervised learning. As for the unsupervised learning, a segmentation term extracted from the Chan-Vese segmentation model [12] is used, with which the learning process can be carried out without labeled training data.

A map is diffeomorphic if its Jacobian is positive everywhere.

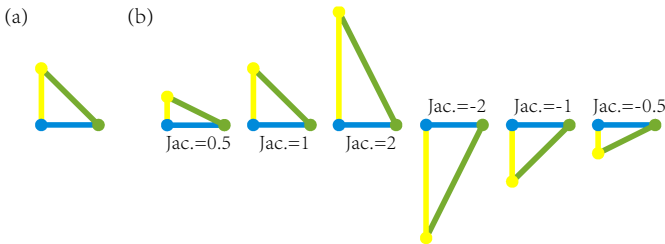


Fig. 3: Illustration of deformations with different values of Jacobian. More deviation from the value of 1 means larger deformation. A negative Jacobian determinant represents an orientation change of the mapping.

The following ReLU Jacobian regularizer is proposed:

$$\mathcal{L}_{Jac}(f) = ||ReLU(-\det \nabla(f))||_1 \quad (7)$$

where $\det \nabla(f)$ denotes the Jacobian determinant of f , $ReLU(\cdot)$ represent the ReLU activation function that set negative values to zero while keeping positive values. As such, the portion of the deformation map with positive Jacobian will not be penalized. Only the portion of the deformation map with negative Jacobian will be adjusted by minimizing the loss function. Fig. 3 illustrates how the orientation of a map can be described by the Jacobian. A triangle in (a) is transformed into the first three triangles in (b), which are all orientation-preserving. In these cases, the Jacobian determinants of the deformation maps are all positive. However, the triangle in (a) is transformed into the last three triangles, which are orientation-reversing. The Jacobian determinants of deformation maps are negative.

To further enhance the smoothness of f , the Laplacian regularization is also adopted:

$$\mathcal{L}_{Lap}(f) = ||\Delta(f)||_1 \quad (8)$$

where $\Delta(f)$ denotes the Laplacian of the mapping f .

For supervised learning, the overall loss function is written as:

$$\mathcal{L} = \mathcal{L}_{Dice}(M_{pred}, M_{label}) + \lambda_{Jac} \mathcal{L}_{Jac}(f) + \lambda_{Lap} \mathcal{L}_{Lap}(f) \quad (9)$$

where $\mathcal{L}_{Dice}(M_{pred}, M_{label})$ are Dice loss.

For unsupervised learning, the fidelity term is adopted from the Chan-Vese segmentation model. The overall loss function can be written as follows:

$$\mathcal{L} = \mathcal{L}_{CV}(I, M_{pred}) + \lambda_{Jac} \mathcal{L}_{Jac}(f) + \lambda_{Lap} \mathcal{L}_{Lap}(f) \quad (10)$$

where $\mathcal{L}_{CV}(I, M_{pred})$ is given by:

$$\mathcal{L}_{CV}(I, M_{pred}) = \int_D (I - c_1 M_{pred} - c_2 (1 - M_{pred})) \quad (11)$$

where $c_1 = \frac{\int_D I * M_{pred}}{\int_D M_{pred}}$ and $c_2 = \frac{\int_D I * (1 - M_{pred})}{\int_D 1 - M_{pred}}$, D is the whole image domain. In fact, c_1 here denotes the mean pixel value of the foreground (region covered by the predicted mask) while c_2 is the mean pixel value of the background.

Multi-level TPSN To enhance the robustness and accuracy of our proposed model, we apply a multi-level strategy to build the *multi-level topology-preserving segmentation network (ml-TPSN)*. The pipeline and architecture of ml-TPSN are shown in Fig. 2. We downsample the original image I into I' and I'' , by $1/2$ and $1/4$ of the original dimension, respectively. I'' is fitted into an encoder-decoder network with a coarse template mask of the same size as I'' to output a predicted segmentation mask. The predicted segmentation mask provides a rough approximation of the segmentation. This coarse predicted mask will be upsampled and used as the template mask M' in the next level for I' . I' and M' are fitted into another encoder-decoder network, and a similar operation is repeated. The whole procedure is completed when the final encoder-decoder outputs a mask M with the exact resolution as the original image I .

Such a multi-level strategy makes it feasible for our model to extract features in a coarse-to-fine manner. A predicted mask is used as the template mask in the next TPSN layer, which is closer to the actual mask. As a result, the model is more robust and can produce more accurate segmentation, especially for structures with complex geometry. This strategy can also effectively prevent getting a sub-optimal solution.

Multi-Objects Segmentation Multi-object segmentation is the segmentation process to extract multiple objects in an image. This is especially useful in medical imaging. Segmenting each individual object by different networks is time-consuming and highly costly. Although pixel-wise segmentation networks for multi-object segmentation are available in the literature [35], such a task has rarely been explored by deformable models. Our proposed TPSN can be naturally applied for multi-object segmentation. For single-object segmentation, the output of the encoder-decoder module is 3 channels (for 3D volume images). For segmenting q objects, the output should be a channel number of $3q$. Each group of 3 channels is used to give the deformation map to deform the associated template to segment the corresponding class of objects in the image.

C. FFDS strategy for multi-genus objects

Evidently, TPSN is capable of segmenting multiply-connected objects. To achieve better results, we propose the Fill First, Dig Second (FFDS) strategy, which is illustrated in Fig. 4. To segment a multiply-connected object, we first use a simply-connected shape and deform the shape to cover the target region. In this stage, the holes in the label mask will be filled. Such an operation simplifies the problem by segmenting a simply-connected shape. After sufficient training in this stage

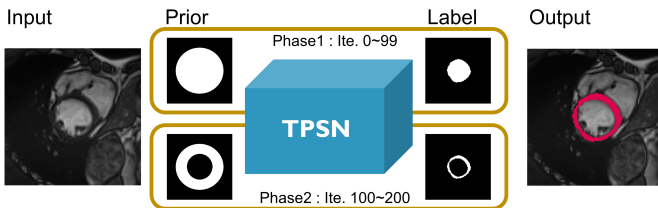


Fig. 4: Illustration of Fill First, Dig Second strategy. A disk without hole is deformed to enclose the filled label mask. A hole will be dug out and further optimized to locate the inner boundary.

(about 100 epochs in our case), the First Dig phase is completed. In the second stage, holes will be removed from the template to acquire the same topology as the objective. The original labeled mask with holes is then used as the training label in this phrase. The main task in this stage is to refine the interior edges of the segment region of interest.

IV. EXPERIMENT

A. Implementation Details

We describe the implementation details in this subsection. The self-ablation study on the weighting parameter of the ReLU Jacobian regularization, as well as the influence of the shape of the prior, will be conducted. We will also examine the effect of the number of levels in the mlTPSN module to determine the optimal number of levels. Furthermore, we will compare our methods with other state-of-art topology-preserving learning-based methods, such as TEDSNet[3] and TeTrIs[9]. The pixel-wise segmentation network, such as the baseline U-Net[7] model and the double U-Net[1] model, will also be compared. The unsupervised TPSN has the same architecture as the supervised TPSN, except that the loss function for the unsupervised model is given by Equation (10). To quantitatively evaluate our methods, we will use the standard Dice score, the Hausdorff distance and the Betti error[32], [34], which is defined as the 0-dimensional Betti number. Finally, as our method is a deformable model that produces the final mask by warping the template by a diffeomorphism, the ReLU Jacobian will be reported to reveal the bijectivity of the mapping.

Dataset Four datasets are used in this work. The 3D volumetric dataset of kidney images [10] is used for the self-ablation study. Among the entire 300 images in the dataset, 210 images are used for training while the remaining 90 images are used for testing. All images are central-cropped and resized to the size of $128 \times 128 \times 64$. The unsupervised TPSN is evaluated on the Ham10000 dataset to segment skin lesions[19], [36]. In this experiment, we will consider the simply-connected lesions only. The 10015 images containing disconnected lesions in the original dataset are removed. They are not included in training and testing. The main purpose is to examine the effectiveness of our model in preserving the topological prior (that is, simply-connected). The final selected dataset contains 9981 images. 8981 of them are used for training, while the remaining 1000 images are used for testing. The images are all resized into a size of 512×512 . To examine our model for segmenting doubly-connected structures, the ACDC [11] dataset is used. The experiments are carried out on 2D images. 5 slices containing circular vessel structures from 100 cases are extracted and used as the dataset. 90 cases are used for training, which comprises of 450 images. Another 10 cases (50 images), which are blind to the network during training, are used for testing. KiTS21[10] dataset is also used for the 3D segmentation of simply-connected structures. The experiment follows the same process as in the self-ablation study. We also evaluate the capability of our methods for multi-objects segmentation[13]. To the best of our knowledge, it is the first learning-based deformable model for multi-object segmentation.

Parameter	Value	Dice	Hausdorff	Betti	\mathcal{L}_{Jac}
λ_{Jac} .	0	93.01	4.34	1.27	27.34
	10^{-2}	92.96	4.12	1.08	0.25
	10^{-1}	92.87	4.08	1.03	0.03
	1.0	92.65	3.86	1.00	0.00
	10^1	92.88	3.84	1.00	0.00
	10^2	89.11	4.41	1.00	0.00
No. of levels	1	92.65	3.86	1.00	0.00
	2	93.21	3.82	1.00	0.00
	3	93.63	3.79	1.00	0.00
	4	93.71	3.79	1.00	0.00
Shape	Disk	92.49	3.91	1.00	0.00
	Ellipse	92.51	3.90	1.00	0.00
	Sqaure	92.38	3.98	1.00	0.00
	Mean Shape	92.65	3.86	1.00	0.00

TABLE I: Self-ablation on ϵ , λ and number of levels for multi-level TPSN

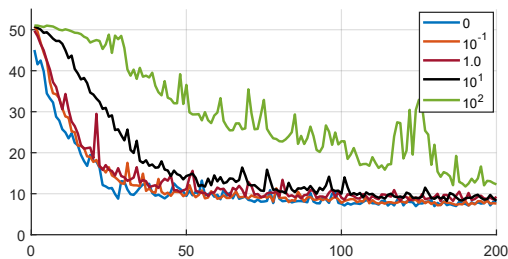


Fig. 5: Convergence Analysis for parameter λ_{Jac} .

The whole 30 cases in the dataset are divided into 25 and 5 for training and testing, respectively. Note that only 8 organs (spleen, right kidney, left kidney, gallbladder, liver, stomach, right adrenal gland, left adrenal gland) are used in this work. For the sake of convenience, all images are centrally cropped and resized into $128 \times 128 \times 128$. The intensity for all images is normalized to $[0, 1]$.

Resources and Parameters All models are trained for 300 epochs with a learning rate of 0.00001 using RMSprop optimizer. A batch size of 8 is used for experiments on KiTS21 and BTCV and 16 is used for experiments on ACDC. The models are trained on a CentOS 8.1 central cluster computing node with two Intel Xeon Gold 5220R 24-core CPU and two NVIDIA V100 Tensor Core GPU. The weighting parameters λ_{Dice} , λ_{Jac} and λ_{Lap} are set to be 1.0, 1.0 and 0.01 respectively, unless specifically indicated.

B. Ablation Study

Our model has several parameters, e.g., the weighting parameter λ_{Jac} . for ReLU Jacobian regularization, the number of levels for mITPSN, and the prior shape used as the template mask. In this subsection, we perform experiments to test how these parameters affect final segmentation results.

Effect of λ_{Jac} . First, to demonstrate the significance of the proposed Jacobian regularization \mathcal{L}_{Jac} , experiments using different weighting parameters λ_{Jac} . are conducted. The segmentation results measured quantitatively by different metrics are reported in TABLE I. More specifically, the following parameters, $\lambda_{Jac} = 0, 10^{-2}, 10^{-1}, 1, 10, 10^2$, have been used. The reported value takes the average results from 5 independent experiments. As indicated in the table, the Jacobian loss without ReLU Jacobian regularization obtained the best by Dice score.

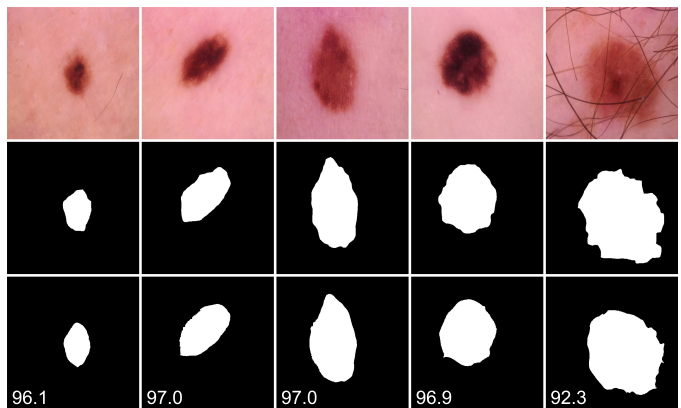


Fig. 6: The results for unsupervised TPSN using the selected HAM10000 dataset. Top: the input image; Middle: the ground truth; Bottom: the predicted mask by unTPSN

Method	Run. Time (s)	Dice	Haus.	Betti	\mathcal{L}_{Jac}
Zhang's	2.87	87.99	9.69	1.00	0.00
unTPSN	0.02	88.15	9.94	1.00	0.00

TABLE II: Quantitative comparison for unsupervised TPSN using the selected HAM10000 dataset.

However, its Hausdorff distance is the worst. The reason is that the topology of the predicted mask contains many isolated regions, which are the topological errors. This is also reflected by the Betti error. With $\lambda_{Jac} = 1.0$, the topology correctness can be achieved without sacrificing the Dice score by too much. The Jacobian loss is reported. As shown in the table, choosing $\lambda_{Jac} \geq 1.0$ is sufficient to keep the Jacobian determinant to be positive and hence bijective. Moreover, if λ_{Jac} . is larger than 10, the segmentation results will be less accurate due to the over-constraint. Fig. 5 illustrate the convergence of the loss function for each λ_{Jac} . It is observed that a larger λ_{Jac} . will slow down the convergence. However, it is acceptable, and the training process generally converges within 200 epochs.

Effect of the number of levels in multi-level TPSN Using $\lambda_{Jac} = 1.0$ and $\lambda_{Lap} = 0.01$, we test the effect of the number of levels used in the multi-level TPSN. The segmentation results are reported in TABLE I. It is observed that the mITPSN with different numbers of levels can all give segmentation results with correct topology. The segmentation results improve from 1 to 3 levels. The results differ slightly between 3 and 4 levels. In this paper, 3-level is used for all the mITPSN experiments.

Effect of the prior shape The robustness of our model under different shapes of the template masks is also investigated. In this experiment, we use four different template shapes, namely, (i) a disk, (ii) an ellipse, (iii) a square, and (iv) the average shape from a dataset. This study is performed on a selected Ham10000 dataset. The quantitative results are given in TABLE I. It is evident that the segmentation results obtained by different template synthetic shapes (that is, shape (i), (ii) and (iii) are similar. Nevertheless, the segmentation results obtained by the mean shape are the best. It demonstrates that a template shape closer to the ground truth can improve segmentation accuracy, which is expected.

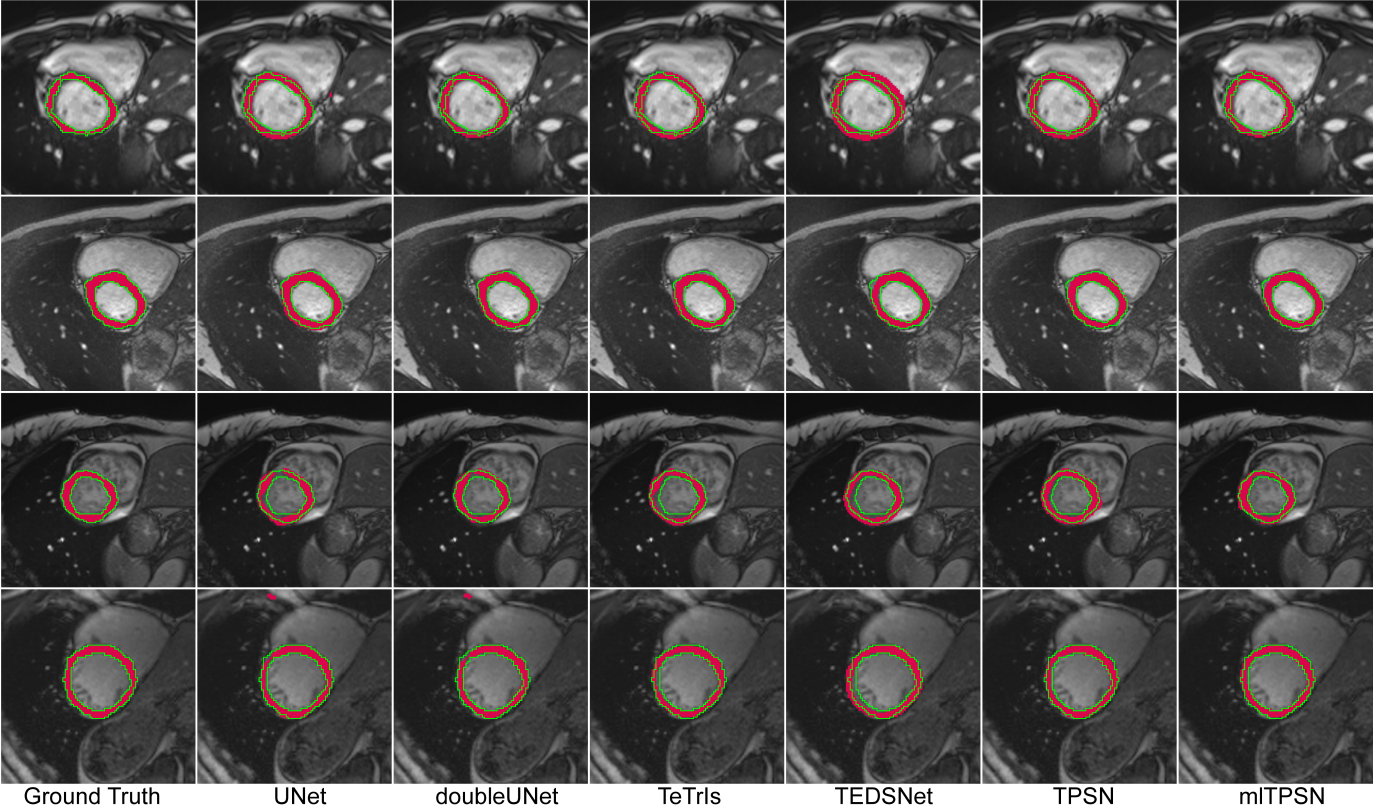


Fig. 7: Segmentation results by different methods for ACDC dataset. The conventional pixel-wise approaches often produced isolated noisy regions (yellow arrow) and discontinuity errors (blue arrow). The other state-of-the-art deformable models result in sub-optimal results due to over-constraint.

C. Unsupervised Segmentation

To validate our proposed unsupervised TPSN(unTPSN) for image segmentation, experiments have been carried out on a selected Ham10000 dataset. unTPSN uses the loss function given by Equation (10). It predicts the segmentation mask based on the intensity information only, without the labeled data. The segmentation results are reported in TABLE II. In comparison, the optimization approach [27] requires 2.87 seconds on average to segment one single image, while unTPSN takes only 0.02 seconds to obtain the segmentation result upon successful training. The qualitative results of unTPSN are given in Fig. 6. The second row shows the ground truth and the third row shows the segmentation results obtained by unTPSN. The Dice scores are reported at the bottom left. It is evident that the segmentation results by unTPSN are satisfactory and comparable to the optimization approach.

D. Comparison with other state-of-the-art methods

In this subsection, we compare our TPSN and mlTPSN with other state-of-the-art learning-based segmentation models, such as the TEDS [3] and TeTrIs[9]. Both simply-connected and doubly-connected structures in 2D and 3D will be segmented to evaluate the performance of our methods.

2D image segmentation We first compare our segmentation results with other state-of-the-art methods for doubly-connected structures in 2D images. For multiply-connected object segmentation, the FFDS strategy described in Section III-C is used.

Dataset	Method	Dice	HD	Betti	\mathcal{L}_{Jac}
ACDC2D	UNet	84.31	2.46	1.08	\
	wUNet	86.10	2.26	1.04	
	TeTrIs	80.26	3.54	1.00	2.49
	TEDSNet	81.54	3.47	1.00	1.46
	TPSN	82.75	2.37	1.00	00.02
	mlTPSN	85.15	2.04	1.00	00.00
KiTS21	UNet	93.41	4.92	1.68	\
	wUNet	94.26	4.48	1.31	
	TeTrIs	91.03	4.44	1.00	0.20
	TEDSNet	90.07	4.27	1.00	0.00
	TPSN	92.65	3.86	1.00	0.00
	mlTPSN	93.63	3.80	1.00	0.00

TABLE III: Comparison with other methods for single-connected component segmentation. Note that in the experiment on 2D ACDC slices (with doubly-connected structures), though FFDS strategy is one of the contributions, it is applied to all deformation-based methods for a fair comparison.

The first phase is carried out during the first 100 epochs to locate the outer boundary. The remaining epochs in the second phase approximate the inner boundary. The results are reported in TABLE III. It is observed that the non-deformation-based segmentation models can acquire better results by Dice score, which benefits from the flexibility of the pixel-wise prediction. In terms of the geometric metric like the Hausdorff distance, the segmentation results are worse due to isolated noisy regions. Regarding the topology correctness, all methods designed for topology-preserving segmentation can give accurate results without topological error. However, the pixel-wise segmentation methods fail to give topology-preserving results. From the table,

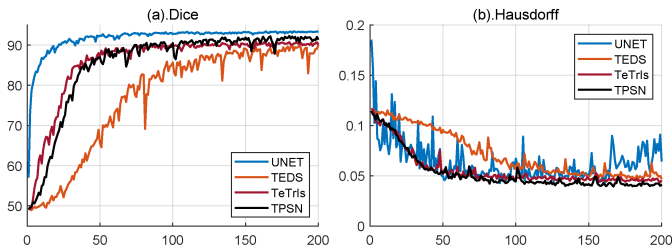


Fig. 8: Convergence analysis for different methods. UNet achieves the best Dice score and the fastest convergence due to the flexibility of segmenting by pixel-wise classification. However, by Hausdorff distance, UNet is the worst due to the lack of proper geometric regularization. Our methods achieved the best by Hausdorff and obtained comparable results by Dice.

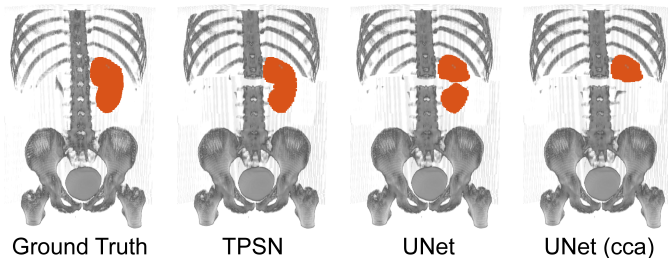


Fig. 9: Segmentation results for 3D segmentation with information loss on KiTS21 dataset. Some slices of the image input for segmentation are missing, resulting in two separate parts by pixel-wise segmentation methods like UNet. Such an issue can not be solved by connected component analysis, as illustrated.

our proposed method achieves the best results quantitatively. TEDSNet[3] performs too much smoothing and results in sub-optimal results due to the over-constrained optimization. TeTrIs[9] uses smoothness as the main regularization, which is not directly related to topology. As such, heavy weighting of the regularization term is needed to ensure the topology correctness.

Figure 7 shows the segmentation results obtained by different methods. As clearly pointed out by the yellow arrow, the non-deformation model, such as UNet and doubleUnet, can easily produce incorrect isolated components, which are far from the object to be segmented. In the third case, it can be observed that both U-Net and double U-Net give segmentation results with topological errors pointed out by the blue arrow. Among the deformation-based models, it is apparent that the segmentation results obtained by TEDSNet and TeTrIs are deviated from the ground truth, although they can maintain the topological correctness. Our methods, TPSN and mTPSN, can give segmentation results comparable to the ground truth without the topological error.

Image segmentation for 3D volumetric images We also test the TPSN and mTPSN on KiTS21 dataset to segment organs from 3D volumetric images. By morphology, the (left/right) kidney is simply-connected with a single component. We use a 3D genus-0 ball as the template mask. In this experiment, only the left kidney with labels will be used. The quantitative results are reported in Table III. The result shows that the pixel-wise segmentation methods generally obtain a higher Dice score but may contain topological errors. The Hausdorff distances are obviously higher. On the other hand, both the

TEDSNet and TeTrIs acquire better results than pixel-wise segmentation models in terms of the Hausdorff distance. However, the Hausdorff distances by the TEDSNet and TeTrIs are significantly bigger than our methods. It may be due to the over-constrained issue. In terms of the topological correctness, all deformable segmentation models can give segmentation results without topological errors.

The convergence of different models in term of different metrics are also analyzed and is given in Figure 8. The plot shows that the pixel-wise segmentation model has a faster convergence. However, the Dice score converges to a smaller value. The convergence of TEDSNet is the slowest among the four methods. In terms of the Hausdorff distance, it is observed that all deformable segmentation models converge in a similar gradual pattern, while the pixel-wise segmentation model shows an unstable non-convergent curve.

We also study the tolerability of our model to information loss after sufficient training. We assume some slices of the scan are missing; thus, some information is missing. The incomplete scans are then fitted into the trained network without processing. The segmentation results obtained by different methods are shown in Figure 9. As shown in the figure, our method can still produce an accurate segmentation result with the correct topology. The segmentation result by UNet has two separate components. Using connected component analysis to correct the topology in such a case gives an even worse result.

E. Multi-object Segmentation

All of the previous experiments focus on the segmentation of a single structure in the image. In this subsection, we examine the performance of our proposed model for multi-object segmentation, which is a fundamental task in medical imaging. In this experiment, the BTCV dataset from MICCAI 2015 Multi-Atlas Abdomen Labeling Challenge[13] is used. The template masks for multiple objects used in this experiment are the bounding boxes for the organs, which can be extracted by detection networks [37]. For a fair comparison, we concatenate the template masks with the original image as the input to provide the same prior information for U-Net and double U-Net. Besides standard TPSN and mTPSN, we also test how the TPSN without ReLU Jacobian loss performs.

The quantitative results are reported in Table IV. Our method achieves the best result among all the models in terms of the average Dice score, even compared to pixel-wise segmentation with the prior input. It demonstrates that the deformation-based segmentation model can acquire better geometric guidance from the shape prior, in the case when the topological priors are known. As in the experiments in the previous sections, our approach can always yield segmentation results with a correct topology. Our method can generally achieve the best in Hausdorff distance for most organs, although it is not as good as double U-Net when segmenting the liver. It may be due to the fact that the liver label masks are highly concave and the deformable segmentation model may sometimes fail to extract the boundary of the liver precisely.

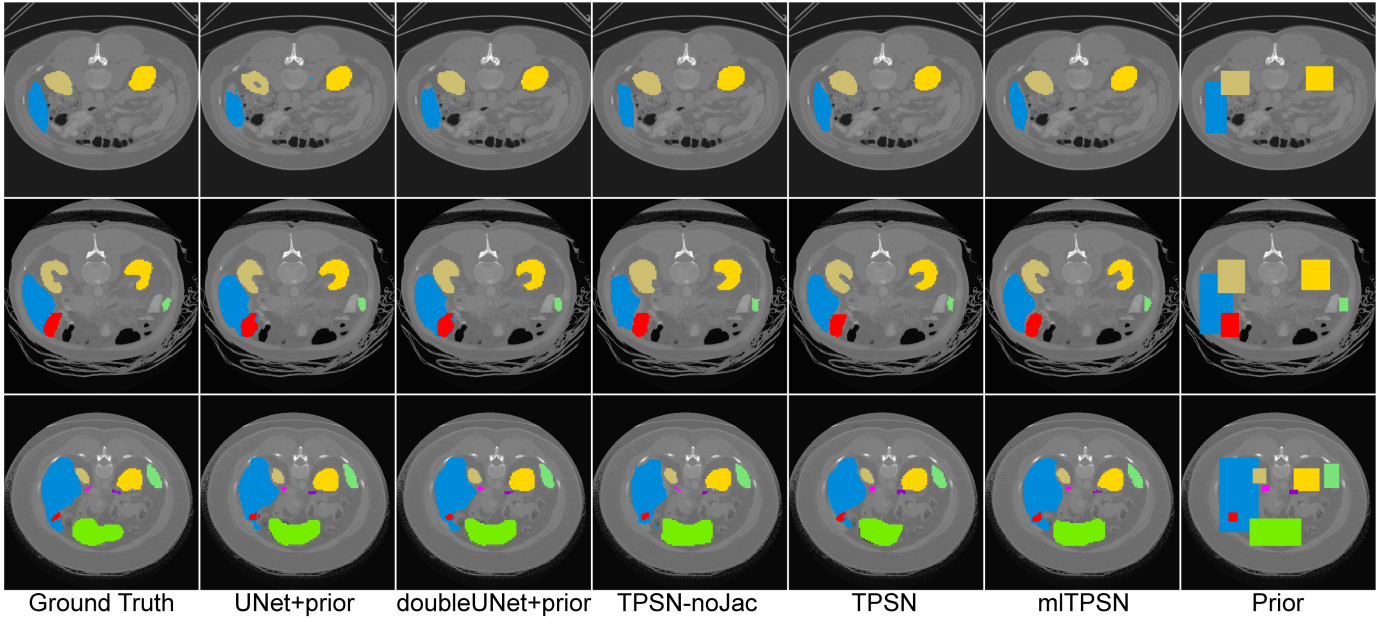


Fig. 10: Segmentation results in comparison with the state-of-the-art methods for BTCV. The results here for UNet and doubleUNet are produced by the experiments with prior input.

Metric	Method	Average	Spl	Kid(R)	Kid(L)	Gall	Liv	Sto	AG(R)	AG(L)
Dice	UNet	62.90	82.59	86.89	82.39	36.06	87.96	52.86	42.87	31.64
	wUNet	67.69	83.33	87.73	84.39	40.94	89.41	61.06	49.12	45.57
	UNet+prior	82.07	87.60	88.79	87.26	78.87	90.08	87.62	65.89	70.43
	wUNet+prior	82.93	89.05	89.45	87.76	81.61	91.27	87.90	66.42	70.00
	TPSN-noJac	82.62	89.61	89.05	88.98	82.81	89.56	87.98	63.67	69.27
	TPSN	82.28	88.45	88.96	88.95	81.07	89.99	86.48	64.98	69.34
	mlTPSN	83.49	89.33	89.10	89.13	82.11	90.43	87.07	68.38	72.40
HD	UNet	10.15	8.14	13.50	6.62	6.27	14.71	18.78	6.58	6.65
	wUNet	9.09	8.81	12.17	5.42	5.11	12.63	16.51	5.43	6.65
	UNet+prior	5.52	5.46	3.87	3.88	3.79	11.50	6.24	3.69	5.78
	wUNet+prior	5.08	5.31	3.50	3.67	3.30	9.44	6.21	3.44	5.81
	TPSN-noJac	5.08	5.80	3.49	3.56	3.66	10.81	6.51	3.72	3.11
	TPSN	5.23	5.28	3.54	3.54	3.31	10.43	7.06	3.47	3.23
	mlTPSN	4.69	5.13	3.33	3.47	3.27	9.97	6.12	3.13	3.06
Betti	UNet	3.27	1.60	5.20	2.00	1.60	5.60	6.20	1.60	2.40
	DoubleUNet	3.00	1.60	4.60	2.00	1.20	4.80	7.00	1.20	1.60
	UNet+prior	2.08	1.20	1.00	1.00	1.40	7.40	2.00	1.40	1.20
	wUNet+prior	1.63	1.20	1.00	1.00	1.40	4.40	1.60	1.20	1.20
	TPSN-noJac	1.13	1.20	1.00	1.00	1.00	1.20	1.00	1.20	1.40
	TPSN	1.00	1.00	1.00	1.00	1.00	1.00	1.00	1.00	1.00
	mlTPSN	1.00	1.00	1.00	1.00	1.00	1.00	1.00	1.00	1.00
\mathcal{L}_{Jac}	TPSN-noJac	0.77	0.67	0.35	0.30	0.49	3.52	0.53	0.14	0.12
	TPSN	0.00	0.00	0.00	0.00	0.00	0.00	0.00	0.00	0.00
	mlTPSN	0.00	0.00	0.00	0.00	0.00	0.00	0.00	0.00	0.00

TABLE IV: Result of multi-object segmentation using the BCTV dataset. Spl: spleen, Kid(R): right kidney, Kid(L): left kidney, Gall: gallbladder, Liv: liver, Sto: stomach, AG(R): right adrenal gland, AG(L): left adrenal gland

V. CONCLUSION

In this work, we proposed a novel learning-based segmentation framework called Topology-Preserving Segmentation Network (TPSN). As a deformable model, our TPSN completes the segmentation task by generating a mapping using an encoder-decoder architecture to transform the template mask into the region of interest. The mapping is regularized by the proposed ReLU Jacobian regularization to be orientation-preserving. With such a mapping, the topology of the transformed mask remains the same as the template. The proposed learning model can either be a supervised model or extended to an unsupervised

segmentation model using an intensity-based loss function adopted from the Chan-Vese model.

Extensive experiments have been carried out to demonstrate the effectiveness of our proposed framework. Self-ablation studies have been done to study the effects of various parameters in the framework. To evaluate the capability of our model in different dimensions, we perform experiments for both 2D planar images and 3D volume images. We also conduct experiments to segment structures with different topologies. Compared with other state-of-art methods, our proposed method promises comparable results by Dice score

and often outperforms others by geometric measures like Hausdorff distance. Moreover, with the carefully designed ReLU Jacobian term, our method can consistently predict segmentation masks with the correct topology.

However, for objects with high concavity, our method cannot achieve results as good as the pixel-wise segmentation method. As the displacement vectors push a smooth edge in the template to a highly concave region in the target, the Jacobian nearby can be large. It can be an explanation for the limitation. To solve this issue, in the future, we will consider the application of quasiconformal theories in the model, which can control the geometric distortion effectively.

REFERENCES

- [1] D. Jha, M. A. Riegler, D. Johansen, P. Halvorsen, and H. D. Johansen, "Doubleu-net: A deep convolutional neural network for medical image segmentation," in *2020 IEEE 33rd International symposium on computer-based medical systems (CBMS)*. IEEE, 2020, pp. 558–564.
- [2] D. Qin, J.-J. Bu, Z. Liu, X. Shen, S. Zhou, J.-J. Gu, Z.-H. Wang, L. Wu, and H.-F. Dai, "Efficient medical image segmentation based on knowledge distillation," *IEEE Trans. on Medical Imaging*, vol. 40, no. 12, pp. 3820–3831, 2021.
- [3] M. K. Wyburd, N. K. Dinsdale, A. I. Namburete, and M. Jenkinson, "Teds-net: Enforcing diffeomorphisms in spatial transformers to guarantee topology preservation in segmentations," in *Proc. of Int. Conf. on Medical Image Computing and Computer-Assisted Intervention*. Springer, 2021, pp. 250–260.
- [4] O. Oktay, E. Ferrante, K. Kamnitsas, M. Heinrich, W. Bai, J. Caballero, S. A. Cook, A. De Marvao, T. Dawes, D. P. O'Regan *et al.*, "Anatomically constrained neural networks (acnns): application to cardiac image enhancement and segmentation," *IEEE Trans. on Medical Imaging*, vol. 37, no. 2, pp. 384–395, 2017.
- [5] H.-L. Chan, S. Yan, L.-M. Lui, and X.-C. Tai, "Topology-preserving image segmentation by beltrami representation of shapes," *Journal of Mathematical Imaging and Vision*, vol. 60, no. 3, pp. 401–421, 2018.
- [6] C. Y. Siu, H. L. Chan, and R. L. Ming Lui, "Image segmentation with partial convexity shape prior using discrete conformality structures," *SIAM Journal on Imaging Sciences*, vol. 13, no. 4, pp. 2105–2139, 2020.
- [7] O. Ronneberger, P. Fischer, and T. Brox, "U-net: Convolutional networks for biomedical image segmentation," in *Proc. of Int. Conf. on Medical Image Computing and Computer-Assisted Intervention*. Springer, 2015, pp. 234–241.
- [8] M. Jaderberg, K. Simonyan, A. Zisserman *et al.*, "Spatial transformer networks," *Proc. of Int. Conf. on Neural Information Processing Systems*, vol. 28, 2015.
- [9] M. C. H. Lee, K. Petersen, N. Pawlowski, B. Glocker, and M. Schaap, "Tetris: Template transformer networks for image segmentation with shape priors," *IEEE Trans. on Medical Imaging*, vol. 38, no. 11, pp. 2596–2606, 2019.
- [10] N. Heller, F. Isensee, K. H. Maier-Hein, X. Hou, C. Xie, F. Li, Y. Nan, G. Mu, Z. Lin, M. Han *et al.*, "The state of the art in kidney and kidney tumor segmentation in contrast-enhanced ct imaging: Results of the kits19 challenge," *Medical Image Analysis*, vol. 67, p. 101821, 2021.
- [11] O. Bernard, A. Lalonde, C. Zotti, F. Cervenansky, X. Yang, P.-A. Heng, I. Cetin, K. Lekadir, O. Camara, M. A. G. Ballester *et al.*, "Deep learning techniques for automatic mri cardiac multi-structures segmentation and diagnosis: is the problem solved?" *IEEE Trans. on Medical Imaging*, vol. 37, no. 11, pp. 2514–2525, 2018.
- [12] T. F. Chan and L. A. Vese, "Active contours without edges," *IEEE Transactions on image processing*, vol. 10, no. 2, pp. 266–277, 2001.
- [13] B. Landman, Z. Xu, J. E. Igelsias, M. Styner, T. R. Langerak, and A. Klein, "2015 miccai multi-atlas labeling beyond the cranial vault – workshop and challenge," *Synapse*, 2015.
- [14] M. Kass, A. Witkin, and D. Terzopoulos, "Snakes: Active contour models," *International journal of computer vision*, vol. 1, no. 4, pp. 321–331, 1988.
- [15] J. MacQueen, "Classification and analysis of multivariate observations," in *5th Berkeley Symp. Math. Statist. Probability*, 1967, pp. 281–297.
- [16] F. Milletari, N. Navab, and S.-A. Ahmadi, "V-net: Fully convolutional neural networks for volumetric medical image segmentation," in *Proc. of Int. Conf. on 3D Vision (3DV)*. IEEE, 2016, pp. 565–571.
- [17] Ö. Çiçek, A. Abdulkadir, S. S. Lienkamp, T. Brox, and O. Ronneberger, "3d u-net: Learning dense volumetric segmentation from sparse annotation," in *Proc. of Int. Conf. on Medical Image Computing and Computer-Assisted Intervention*. Springer, 2016, pp. 424–432.
- [18] Z. Zhou, M. M. Rahman Siddiquee, N. Tajbakhsh, and J. Liang, "Unet++: A nested u-net architecture for medical image segmentation," in *Deep learning in medical image analysis and multimodal learning for clinical decision support*. Springer, 2018, pp. 3–11.
- [19] P. Tschandl, C. Rosendahl, and H. Kittler, "The ham10000 dataset, a large collection of multi-source dermatoscopic images of common pigmented skin lesions," *Scientific Data*, vol. 5, no. 1, pp. 1–9, 2018.
- [20] F. Isensee, P. F. Jaeger, S. A. Kohl, J. Petersen, and K. H. Maier-Hein, "nnu-net: A self-configuring method for deep learning-based biomedical image segmentation," *Nature Methods*, vol. 18, no. 2, pp. 203–211, 2021.
- [21] A. Hatamizadeh, Y. Tang, V. Nath, D. Yang, A. Myronenko, B. Landman, H. R. Roth, and D. Xu, "Unetr: Transformers for 3d medical image segmentation," in *Proceedings of the IEEE/CVF Winter Conference on Applications of Computer Vision*, 2022, pp. 574–584.
- [22] A. Dosovitskiy, L. Beyer, A. Kolesnikov, D. Weissenborn, X. Zhai, T. Unterthiner, M. Dehghani, M. Minderer, G. Heigold, S. Gelly *et al.*, "An image is worth 16x16 words: Transformers for image recognition at scale," *arXiv preprint arXiv:2010.11929*, 2020.
- [23] Y. Ouali, C. Hudelot, and M. Tami, "Autoregressive unsupervised image segmentation," in *Proc. of Euro. Conf. on Computer Vision*. Springer, 2020, pp. 142–158.
- [24] W. Kim, A. Kanazaki, and M. Tanaka, "Unsupervised learning of image segmentation based on differentiable feature clustering," *IEEE Trans. on Image Processing*, vol. 29, pp. 8055–8068, 2020.
- [25] T. F. Cootes, C. J. Taylor, D. H. Cooper, and J. Graham, "Active shape models-their training and application," *Computer Vision and Image Understanding*, vol. 61, no. 1, pp. 38–59, 1995.
- [26] D. Zhang and L. M. Lui, "Topology-preserving 3d image segmentation based on hyperelastic regularization," *Journal of Scientific Computing*, vol. 87, no. 3, pp. 1–33, 2021.
- [27] D. Zhang, X.-c. Tai, and L. M. Lui, "Topology-and convexity-preserving image segmentation based on image registration," *Applied Mathematical Modelling*, vol. 100, pp. 218–239, 2021.
- [28] N. K. Dinsdale, M. Jenkinson, and A. I. Namburete, "Spatial warping network for 3d segmentation of the hippocampus in mr images," in *Proc. of Int. Conf. on Medical Image Computing and Computer-Assisted Intervention*. Springer, 2019, pp. 284–291.
- [29] Q. Zeng, D. Karimi, E. H. Pang, S. Mohammed, C. Schneider, M. Honarvar, and S. E. Salcudean, "Liver segmentation in magnetic resonance imaging via mean shape fitting with fully convolutional neural networks," in *Proc. of Int. Conf. on Medical Image Computing and Computer-Assisted Intervention*. Springer, 2019, pp. 246–254.
- [30] A. Mosinska, P. Marquez-Neila, M. Koziński, and P. Fua, "Beyond the pixel-wise loss for topology-aware delineation," in *Proc. of IEEE/CVF Conf. on Computer Vision & Pattern Recognition*, 2018, pp. 3136–3145.
- [31] Y. Zhou, Z. Li, S. Bai, C. Wang, X. Chen, M. Han, E. Fishman, and A. L. Yuille, "Prior-aware neural network for partially-supervised multi-organ segmentation," in *Proc. of Int. Conf. on Computer Vision*, 2019, pp. 10 672–10 681.
- [32] X. Hu, F. Li, D. Samaras, and C. Chen, "Topology-preserving deep image segmentation," *Proc. of Int. Conf. on Neural Information Processing Systems*, 2019.
- [33] S. Shit, J. C. Paetzold, A. Sekuboyina, I. Ezhov, A. Unger, A. Zhylyka, J. P. Pluim, U. Bauer, and B. H. Menze, "cldice-a novel topology-preserving loss function for tubular structure segmentation," in *Proc. of IEEE/CVF Conf. on Computer Vision & Pattern Recognition*, 2021, pp. 16 560–16 569.
- [34] J. Clough, N. Byrne, I. Oksuz, V. Zimmer, J. Schnabel, and A. King, "A topological loss function for deep-learning based image segmentation using persistent homology," *IEEE Trans. Pattern Analysis & Machine Intelligence*, 2020.
- [35] E. Gibson, F. Giganti, Y. Hu, E. Bonmati, S. Bandula, K. Gurusamy, B. Davidson, S. P. Pereira, M. J. Clarkson, and D. C. Barratt, "Automatic multi-organ segmentation on abdominal ct with dense v-networks," *IEEE Trans. on Medical Imaging*, vol. 37, no. 8, pp. 1822–1834, 2018.
- [36] P. Tschandl, C. Rinner, Z. Apalla, G. Argenziano, N. Codella, A. Halpern, M. Janda, A. Lallas, C. Longo, J. Malvehy *et al.*, "Human-computer collaboration for skin cancer recognition," *Nature Medicine*, vol. 26, no. 8, pp. 1229–1234, 2020.
- [37] M. Baumgartner, P. F. Jäger, F. Isensee, and K. H. Maier-Hein, "nndetection: A self-configuring method for medical object detection," in *Proc. of Int. Conf. on Medical Image Computing and Computer-Assisted Intervention*. Springer, 2021, pp. 530–539.